


Nontrivial nanostructure, stress relaxation mechanisms, and crystallography for pressure-induced Si-I \rightarrow Si-II phase transformation

Hao Chen¹, Valery I. Levitas^{2,3} , Dmitry Popov⁴  & Nenad Velisavljevic^{4,5}

Crystallographic theory based on energy minimization suggests austenite-twinned martensite interfaces with specific orientation, which are confirmed experimentally for various materials. Pressure-induced phase transformation (PT) from semiconducting Si-I to metallic Si-II, due to very large and anisotropic transformation strain, may challenge this theory. Here, unexpected nanostructure evolution during Si-I \rightarrow Si-II PT is revealed by combining molecular dynamics (MD), crystallographic theory, generalized for strained crystals, and in situ real-time Laue X-ray diffraction (XRD). Twinned Si-II, consisting of two martensitic variants, and unexpected nanobands, consisting of alternating strongly deformed and rotated residual Si-I and third variant of Si-II, form {111} interface with Si-I and produce almost self-accommodated nanostructure despite the large transformation volumetric strain of -0.237 . The interfacial bands arrest the {111} interfaces, leading to repeating nucleation-growth-arrest process and to growth by propagating {110} interface, which (as well as {111} interface) do not appear in traditional crystallographic theory.

¹Key Laboratory of Pressure Systems and Safety, Ministry of Education, School of Mechanical and Power Engineering, East China University of Science and Technology, Shanghai 200237, People's Republic of China. ²Iowa State University, Departments of Aerospace Engineering and Mechanical Engineering, Ames, IA 50011, USA. ³Ames Laboratory, Division of Materials Science and Engineering, Ames, IA, USA. ⁴HPCAT, X-ray Science Division, Argonne National Laboratory, Lemont, IL, USA. ⁵Physics Division, Lawrence Livermore National Laboratory, Livermore, CA 94550, USA. email: vlevitas@iastate.edu; dpopov@anl.gov

One of the challenging goals in studying high-pressure PTs in materials is finding real time microstructure evolution. This includes crystallographic features of PT, orientation of interfaces, morphology of phases, and stress relaxation mechanisms. Crystallographic theory based on energy minimization^{1,2} suggests austenite-twinned martensite interfaces with specific orientation, which are confirmed experimentally for various materials. For phases that do not exist in the stress-free state, including Si-II, in situ measurements are vital and essential in studying high-pressure PTs. High pressure Laue diffraction is a powerful tool to investigate microstructure evolution across PT in situ^{3–5}, however, a broader application of this powerful experimental capability also requires a strong collaboration with modeling and theory work. Martensitic PT from Si-I to Si-II occurring at 12–14 GPa is studied broadly^{3,5–10}. Si-I/Si-II interface is observed but not uniquely indexed with Laue diffraction, and twinning in Si-II is mentioned hypothetically by Popov et al.⁵. However, MD simulations^{11–13} do not show twinned Si-II. MD simulations reveal atomic features of PT at nm-ps resolution. However, due to limitations of small process duration (ns), sample size (μm), and high strain rate (ps^{-1}), MD stress relaxation mechanisms and nanostructure may deviate from reality. XRD, due to spatial resolution of few micrometers and time resolution of few minutes may miss some finer features and transitional processes. Also, it does not allow unambiguous indexing of interfaces without some assumptions. Here, we show major agreement between these two approaches for the revealed counterintuitive nanostructure, which is very nontrivial and strongly supports both.

Crystallographic theory^{1,2} for cubic-tetragonal PT suggests that there are three tetragonal martensitic variants of Si-II with transformational deformation gradients (i.e., for neglected elastic strains) in cubic coordinates $\mathbf{F}_t^1 = \{a; a; b\}$, $\mathbf{F}_t^2 = \{a; b; a\}$, $\mathbf{F}_t^3 = \{b; a; a\}$, where $a = 1.175$ and $b = 0.553$ ¹¹, i.e., transformation strains ($a - 1$ and $b - 1$) are large, including large transformation volumetric strain $\epsilon_v = \det \mathbf{F}_t - 1 = -0.237$. Each pair of Si-II variants are in twin relation with each other with a $\{110\}$ twinning plane of Si-I lattice and very large twinning shear $\gamma = 1.655$ ¹. Si-I and the mixture of two twin-related Si-II martensitic variants are compatible (i.e., satisfies the Hadamard compatibility condition that follows from the displacement continuity across a coherent interface) for an interface with unit normal $\mathbf{m} = [0.631; 0.754; 0.183]$. Also, complete self-accommodating mixture of martensitic variants (i.e., mixture that occupies region of the same size and shape as the parent phase) within austenitic matrix (e.g., in diamond-shape region),

which does not generate any long-range stresses, requires zero volumetric strain¹, i.e., it is impossible for Si-II.

In this work, we hypothesize that large strains may lead to microstructure and stress relaxation mechanisms, that do not follow traditional crystallographic theories. Each experimental and simulation method has its own pros and cons and cannot give a complete picture. We combine crystallographic theory (which we expand to the deformed crystals and complex nanostructures), MD, and in situ synchrotron radiation diffraction, and reveal unexpected nanostructure evolution during Si-I to Si-II PT, which contradicts the classical crystallographic theory. All three approaches revealed twinned Si-II with the same twinning planes $\{110\}$. Twinned Si-II, consisting of two martensitic variants, and unexpected nanobands, consisting of alternating strongly deformed and rotated residual Si-I and the third variant of Si-II, form $\{111\}$ interface with Si-I and produce almost self-accommodated nanostructure despite the large transformation volumetric strain. The interfacial bands arrest the $\{111\}$ interfaces, leading to repeating nucleation-growth-arrest process and to growth by propagating $\{110\}$ interface, which (as well as $\{111\}$ interface) do not appear in traditional crystallographic theory. Thus, in contrast to classical theory requiring stress-free interfaces, microstructure is governed by reduction of the long-range stresses in the entire volume, tolerating high short-range stresses at complex interfaces, which are necessary to keep residual Si-I and reduce resultant volume jump.

Results

Computational scheme for MD simulations is presented in Fig. 1 and supplementary material. Si-I sample includes two dislocations, which cause stress concentration (Fig. 1), and is loaded by hydrostatic pressure. In the theory¹⁴, single-variant martensite nucleates first and, after reaching some critical size, is then observed to twin. Here, twinned Si-II appears from the beginning (Fig. 1 and Supplementary Movie 6) near each dislocation. In XRD experiment twinning in Si-II is observed from small angles between $\langle 211 \rangle$ and $\langle 220 \rangle$ directions (Fig. 2 and Supplementary Movie 5), consistent with angle up to 8.3° obtained here with the crystallographic theory under strains. In MD simulations with a dislocation dipole (practically two independent single dislocations), pressure for initiation of Si-I \rightarrow Si-II PT is lower than for dislocation-free crystal by a factor of 1.45. In reality, the defect-free Si-I should transform to Si-II at 18.3 GPa, when the first phonon instability in the first principle calculations is observed⁹. Then the observed PT pressure in the current experiment, ~ 13 GPa (see Supplementary Material), which matches the

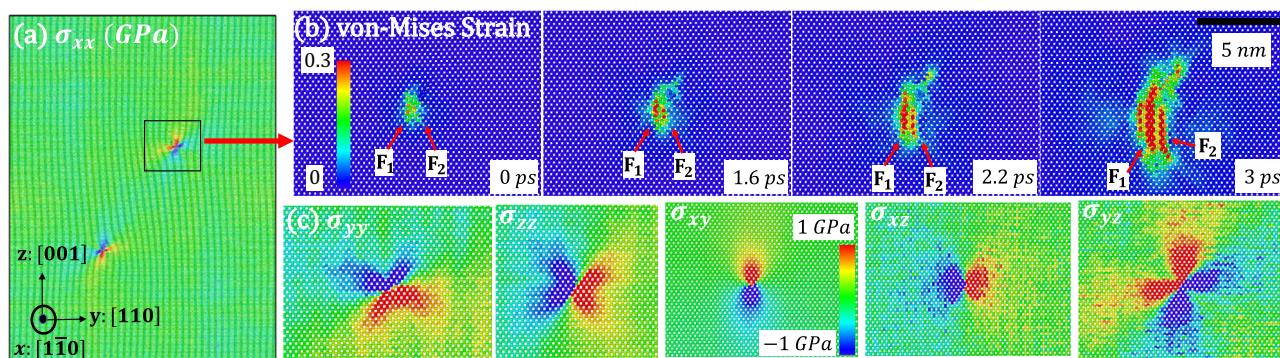


Fig. 1 Field of internal stresses due to dislocations and nucleation of twinned Si-II at two dislocations. **a** Computational model of a single Si crystal with shuffle 60° dislocation dipole inserted by employing dislocation displacement²⁷ at constant hydrostatic pressure, including internal stress distribution due to dislocations. Stress fields of dislocations practically do not overlap. **b** Evolution of von-Mises strain distribution. **c** Distribution of all internal stresses due to dislocation from MD simulation. The twinned Si-II nucleates from single dislocation from the beginning and grows along the $[110]$ (i.e., y) direction. The (110) twinning plane is consistent with the prediction from crystallographic theory¹ and the current experiment.

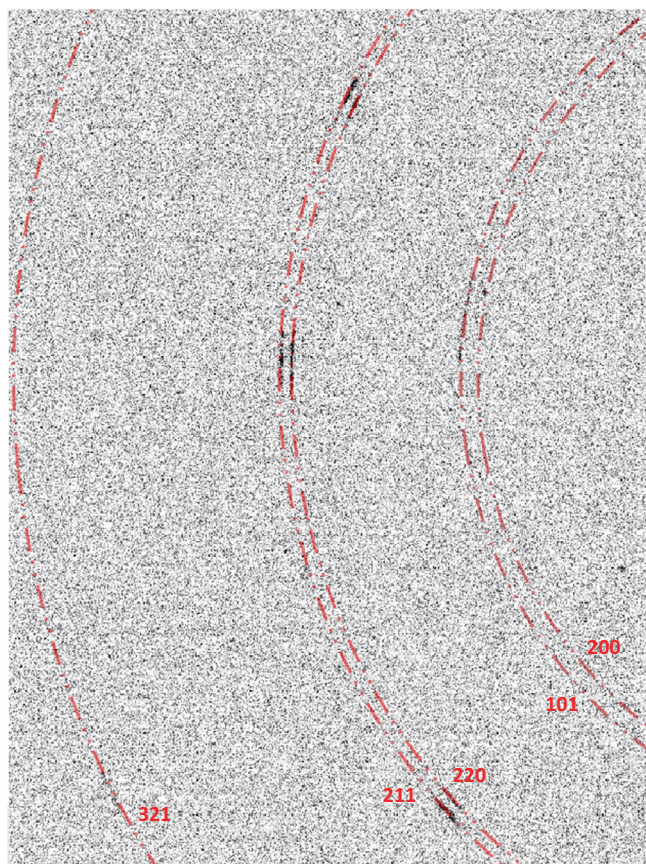


Fig. 2 Oscillation diffraction pattern from Si-II obtained with monochromatic beam in 1° angular range. Red circles denote predicted diffraction lines of Si-II.

typically reported pressures^{3,5–10}, is lower than 18.3 GPa by a factor of 1.41. Thus, a typical nucleation event in the experiment should occur at a single dislocation, consistent with low dislocation density in our Si-I sample. This contrasts with the statement in⁹ that due to the large difference between calculated PT pressure 18.3 and 13 GPa in the experiment, phonon instability cannot be responsible for the initiation of PT; clearly, the effect of dislocations was missed. Another qualitative confirmation of the strong effect of defects on nucleation pressure in our experiments comes from the fact that there are irregular parts of a sample where nucleation did not occur at all because they are probably dislocation-free (see Supplementary Information).

After nucleation, nontrivial microstructure evolution is observed, as shown in Fig. 3 and Supplementary Movie 6. Both in MD and experiment (see below) Si-I and complex Si-II microstructure form a rational interface $\{111\}$, which smallest deviation from predicted by crystallographic theory normal \mathbf{m} is 25.16° . In elasticity-based theory of martensite^{15–17}, a thin layer of alternating tips of twin-related F_t^1 and F_t^2 variants produce significant elastic energy. Due to very large twinning shear of 1.655 for Si-II as well as significant deviation of $\{111\}$ interface from \mathbf{m} , the elastic energy relaxes by producing an unexpected interfacial nanoband II, consisting of alternating F_t^3 variant of Si-II and strongly deformed and rotated residual Si-I (Fig. 3). Such an interfacial band was not observed for any PT in any material and represents nontrivial structural mechanism of internal stress relaxation. These interfacial bands II strongly reduce mobility of the twinned Si-II–Si-I interfaces $\{111\}$, which practically do not propagate. Microstructure evolves in two main ways (Fig. 3 and Supplementary Movie 6). (a) Lengthening of twinned Si-II and

interfacial bands along the bands in $[11\bar{2}]$ direction. During this process, the bands form an interface between Si-I and Si-II close to (110) twin interface, which does not appear in crystallographic theory but is observed in our Laue diffraction experiment (see below). (b) New twinned Si-II nucleates and grows from an interfacial band II, producing next band I and then II. At the same time, previously formed bands I and II keep growing causing movement of (110) interface between Si-I and Si-II.

Using real-time Laue diffraction, we explicitly observed propagation of Si-I/Si-II interfaces, as projected onto a $\{110\}$ plane (Fig. 4a, b and supplementary movies 1, 2, and Supplementary Information). The observed interfaces are parallel to $[101]$ and $[010]$ directions and, at the same time, the interfaces are tilted by large angles with respect to the plane of projection $(10\bar{1})$. It is important to stress that normal to the interface parallel to $[101]$ is oriented far away from the normal $\mathbf{m} = [0.631; 0.754; 0.183]$ predicted by crystallographic theory. The area of the newly formed Si-II overlaps with the area of the rest of Si-I indicating that at least one of these interfaces is tilted by angle of about 45° with respect to the plane of projection. Thus, possible orientations of Si-I/Si-II interfaces include $\{111\}$ and $\{110\}$ interfaces predicted by the MD simulations but do not exclude other directions. The Si-I/Si-II interface in projection on a $\{100\}$ plane was observed in in situ Laue diffraction experiment⁵, but it was not uniquely indexed and, apart from the current results, it was not clear whether Si-II areas grow. Thus, Si-II areas, as projected onto a $\{100\}$ plane, are elongated parallel to a $\langle 110 \rangle$ direction indicating limited range of crystallographic planes, tilted by large angles with respect to the plane of projection and parallel to this $\langle 110 \rangle$ direction. Therefore, possible orientations of Si-I/Si-II interfaces also include $\{111\}$ and $\{110\}$ interfaces predicted by the MD simulations but also still do not exclude other directions. Results⁵ did not reliably exclude interface with normal $\mathbf{m} = [0.631; 0.754; 0.183]$ predicted by crystallographic theory, in contrast to the current results. Si-II produces much broader and “streaky” reflections comparing to the parental phase. This is the indication of substantial misorientation of various nanodomains in Si-II, to some extent like those observed in Fig. 3. Since in⁵ and here the same Si-I/Si-II interfaces are observed as projected onto different crystallographic planes, combining results can yield 3D orientations of the interfaces based solely on the experimental results under the following assumption. Since only interfaces parallel to rational axes with indices 0 or 1 have been observed, it is reasonable to suppose that the interfaces are parallel to rational crystallographic planes with the same kind of indices. This yields interfaces parallel to $\{110\}$ and $\{111\}$ predicted by the MD. As predicted, twinned Si-II and interfacial bands grow along the bands in $[12\bar{1}]$ direction causing shift of the Si-I/Si-II interfaces parallel to (101) and $(1\bar{1}1)$ (Fig. 4c). While interfacial nanobands so far have not been confirmed in experiment due to very small size and severe distortions from cubic Si-I and tetragonal Si-II lattices, experimental confirmation of unexpected $\{111\}$ and $\{110\}$ interfaces, which are directly related to them, makes this unexpected evolving nanostructure plausible.

Discussion

To better understand the reasons for the unusual $\{111\}$ interface, new interfacial bands, presence of residual Si-I deeply in the region of stability of Si-II, and two-band structures with specific spacing, we expanded traditional stress-free crystallographic theory for finite elastic strains (stresses) and evaluated degree of violation of the averaged Hadamard compatibility condition for each of the interface. As a measure of violation, we evaluate the principal components of 2D incompatibility strain tensor \mathbf{Inc} (defined in Supplementary Material) that deform $\{111\}$ interfaces between different phases or bands. For compatible interface

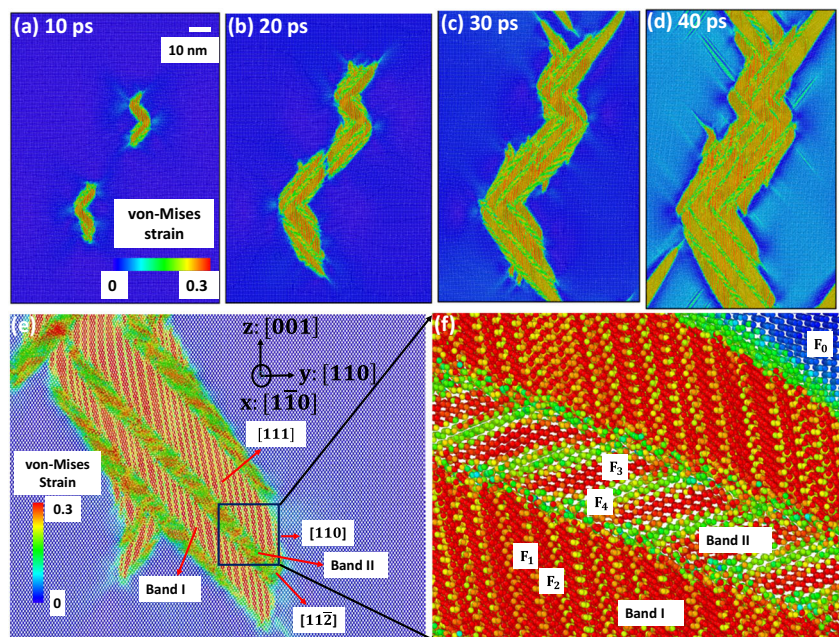


Fig. 3 Snapshot of Si-II microstructure and its rotated and enlarged views. **a–d** The evolution of the microstructure growing from two dislocation-induced nuclei. **e** and **f** The zoomed microstructures composed of the band I, consisting of alternating Si-II variants with deformation gradients F_1 and F_2 (which include elastic strains), separated by (110) twinning plane, and interfacial band II, consisting of alternating Si-II variant F_3 and strongly deformed Si-I with deformation gradient F_4 . The interfaces between the two bands and between Si-I and band II are (111) planes. Another interface between twinned Si-II and Si-I is (110); both are not present in the crystallographic theory¹. Growth occurs by propagation of (110) interface along the bands in [112] direction and by nucleation and growth of new twinned Si-II from an interfacial band II, producing next band I and then band II, as observed in the experimental measurement.

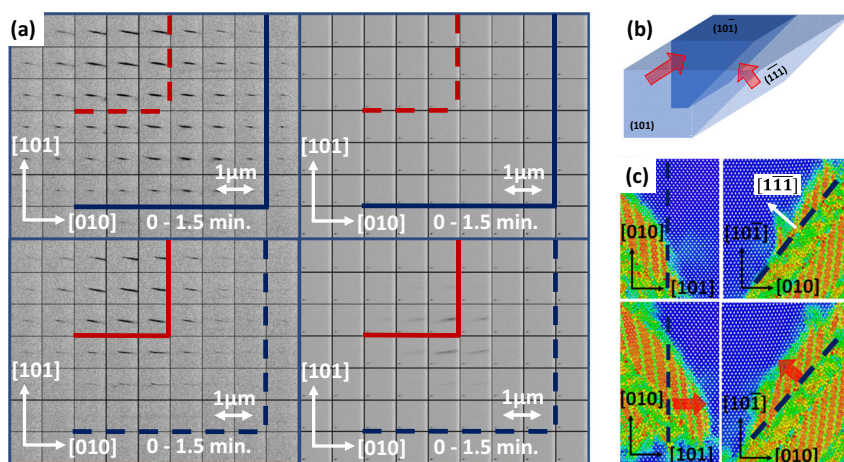


Fig. 4 Shifts of Si-I/Si-II interfaces as observed by in situ real-time Laue diffraction and MD simulation. **a** Maps of 202 reflection from a Si-I crystal (left column) and maps of a diffuse reflection from Si-II (right column). More maps are available in the Supplementary Movie 1. **b** 3D schematic of the shifts of the Si-I/Si-II interfaces. **c** Simulated shifts of the Si-I/Si-II interfaces. In all the images the interfaces before the shifts are shown by dark blue and the interfaces after the shifts are shown by red lines; solid lines denote currently existing interfaces and dotted dashed lines denote interfaces existing in different states; directions of the shifts of the interfaces are shown by red arrows.

$\mathbf{Inc} = (0; 0)$. Thus, for the band I-Si-I interface, $\mathbf{Inc} = (0.069; 0.087)$, i.e., corresponding strains are finite (i.e., on the order of 0.1), which along with local stresses due to alternating twin tips cause nucleation of the band II. For the band II-Si-I interface, $\mathbf{Inc} = (0.117; 0.258)$, which causes much higher local stresses. For the band I-band II interface, $\mathbf{Inc} = (0.326; 0.201)$, which leads to huge local stresses. Thus, incompatibility analysis only increased perplexity: why does the system choose such sophisticated highly energetic nanostructure? However, these interfacial stresses are short-range and partially relaxed by local atomic rearrangements and loss of coherence

(Fig. 3b). Most importantly, (a) averaged over the bands I and II deformation gradient ($F_{av} = \lambda_i F_i$ with volume fractions $\lambda_1 = \lambda_2 = 0.3742, \lambda_3 = 0.1740, \lambda_4 = 0.1126$) produces with Si-I very small incompatibility $\mathbf{Inc} = (0.004; 0.021)$; (b) normal to the {111} interface strain $F_{av} - F_0$ is also small (-0.032); (c) difference in volumetric deformation gradients $\det F_{av} = 0.718$ and $\det F_0 = 0.763$ is -0.045 , i.e., small (in comparison with $\epsilon_v = 0.237$) as well. All these facts produce almost self-accommodated bands I + II nanostructure with small averaged strain within Si-I matrix, and consequently, small long-range internal stresses. The known self-accommodated diamond

microstructure in unstressed shape memory alloys requires zero transformation volume strain and is produced by twin-within-twin structures of the martensite only. Since conditions here are very different (finite elastic deformation of both phases, large transformation volumetric strain $\epsilon_v = 0.237$, very large twinning shear of 1.655), this leads to completely different almost self-accommodated bands I + II nanostructure, which tolerates significant local interfacial incompatibilities, and involves strongly distorted metastable Si-I with F_4 to reduce volumetric difference with hydrostatically deformed Si-I. This determines specific spacing (relative volume fraction) of bands I and II and their unusual {111} interfaces. Thus, huge internal stresses, in particular caused by third variant, are necessary to retain Si-I deeply in the region of stability of Si-II. This mechanism is consistent with the later stage of the PT (Fig. S1 and Supplementary Movie 6): with reducing volume fraction of remaining Si-I matrix and the elastic constraint due to the matrix, volume fractions of band II and of the variant F_3 (λ_3) reduce, and after Si-I matrix disappeared, band II disappears as well leaving twinned Si-II and relaxing elastic stresses. Significant relaxation of lattice distortions in Si-II after completing PT was observed with XRD as well, indicated by “streaky” Laue and arch-like monochromatic beam reflections (Fig. 2). Thus, despite very different time and space scales in MD simulations and experiments, they show surprising and very nontrivial agreement in microstructure and crystallography.

Strong local stress concentrator at the intermediate band II in Si may be a cause for complex polymorphism of Si, leading under different types of loadings and defects to different phases (Si-III, IV, V, VIII, IX, XI, and XII, as well as amorphous Si). Understanding and controlling these stresses and nanostructure may lead to controlling selection of desired known and new (hidden) phases. Obtained combined in situ experimental, MD, and theoretical approaches open opportunities to study other high-pressure PTs in Si and Ge and other materials with large transformations strains, e.g., C, BN, and BCN systems (e.g., -0.39 for PT graphite to diamond or hexagonal to cubic or wurtzitic BN). Obtained results also challenge modern phase field approaches^{18–20} so that they can describe the revealed nanostructures.

Methods

Simulation method. In this work, classical MD simulations were performed using the LAMMPS package²¹. Simulations have been carried out at two constant temperatures, 1 and 300 K, using the Nosé–Hoover thermostat, and for multiple geometries; the obtained nanostructure and even pressure for initiation of PT were the same. The employed interatomic force field for the interactions between Si atoms was from the Tersoff interatomic potential²². This potential has been demonstrated to be successful in describing the crystal structure transition from the diamond-cubic to β -Sn in single crystal silicon (Si-I to Si-II) under a uniaxial stress of ~ 12 GPa¹⁰, which is close to the experimental value^{5–7}. The advantage of the Tersoff interatomic potential for the description of Si-I to Si-II phase transformation in comparison with four other potentials is demonstrated in¹².

We are interested in introducing a single dislocation as a nucleation site for the initiation of the Si-I–Si-II PT. However, to minimize its effect on the periodic boundary conditions at the boundaries, dislocation dipole must be placed with equal in magnitude but opposite Burgers vectors^{23,24}. To reduce the effect of one dislocation on the stress concentrator from another one, distance between dislocations should be maximized. Figure 1a shows the computer model set-up of a single crystalline silicon with static shuffle 60° dislocation dipole with Burgers vector $b = 1/2[1\bar{1}0]$ inserted by imposing the displacement field of dislocations¹³. The dislocation dipole was put on the diagonal of the yz plane to maximize the distance of the two dislocations. The dislocation internal stress field is shown in Fig. 1a, c and is consistent with theoretical predictions¹³. Periodic boundary conditions are applied along all three cubic directions to exclude free surface effect. One of the simulation cells has dimensions of $L_y \approx 99.7$ nm and $L_z \approx 130$ nm and the distance between dislocations of about 82.01 nm. The length L_x has been varied at 1 K from 4 to 30 nm, with a sample containing around 2.5 million to 15 million atoms, and the results are found to be independent of this length due to the periodic boundary conditions applied. Another simulation cell has dimensions of $L_y \approx 199.4$ nm, $L_z \approx 260$ nm, and $L_x \approx 4$ nm, with the distance between dislocations of 164.02 nm containing around 10 million atoms and the

microstructure and the obtained at 300 K nanostructure and pressure for initiation of the PT we the same as for smaller sample and 1 K. Thus, the effect of one dislocation on the nucleation processes at another dislocation is negligible, and our results can be interpreted as nucleation and growth at a single dislocation. The pressure was applied to the system using the Berendsen algorithm²⁵, in which the instantaneous stress of the system was calculated using the virial formula.

Experimental method. High pressure Laue diffraction experiments have been conducted using experimental setup available at 16 BMB beamline of Advanced Photon Source³. Incident polychromatic beam, with the highest X-ray energy limit about 90 keV, reached the sample through one of the diamonds while the diffracted beams reached Perkin Elmer area detector, positioned at about 600 mm from the sample and tilted vertically by 30° , through the other diamond. X-ray incident beam was focused using KB-mirrors down to $3 \times 3 \mu\text{m}^2$ at the half width of beam profiles. The sample was cut manually from the same Si wafer (University Wafer²⁶) as for the previous research⁵ and had dimensions about $15 \times 40 \mu\text{m}^2$. The sample was put into a diamond anvil cell (DAC), having total opening of 60° , such that the nearly flat surface parallel to a {110} plane was also parallel to plane of one of the diamond anvils. The DAC was tilted vertically by 25° providing reasonable number of reflections for indexation. Series of two dimensional (2D) translational scans were collected on the sample across the transition with vertical translations along [101] direction parallel to the longest sample dimension. The 2D scans were collected on an area within the sample heaving size $10 \times 10 \mu\text{m}^2$ with $1 \mu\text{m}$ step in both directions, in 2.5 min each. Precise sample orientation with respect to the translational axes was determined at pressure right below the PT by indexation of diffraction patterns: [101] direction of the sample deviated by about 12° from the vertical axis of translation and [010] direction of the sample deviated by about 3° from the horizontal axis of translation. Therefore, all the details of PT were projected onto a {110} plane with vertical axis of translation nearly parallel to a $\langle 110 \rangle$ direction and horizontal axis of translation nearly parallel to a $\langle 100 \rangle$ direction. Other details of experiment and data analysis are available in supplementary materials.

Data availability

The data that support the findings of this study are available from the corresponding authors upon request.

Code availability

Software polyLaue to analyze Laue diffraction data is available from its author upon reasonable request. Molecular dynamics simulation software LAMMPS is available from its website.

Received: 9 July 2021; Accepted: 24 January 2022;

Published online: 21 February 2022

References

- Bhattacharya, K. *Microstructure of Martensite. Why it Forms and How It Gives Rise to the Shape-Memory Effect* (Oxford University Press, 2003).
- Ball, J. M. & James, R. D. Fine phase mixtures as minimizers of energy. *Arch. Ration. Mech. Anal.* **100**, 13–52 (1987).
- Popov, D., Velisavljevic, N. & Somayazulu, M. Mechanisms of pressure-induced phase transitions by real-time Laue diffraction. *Crystals* **9**, 672 (2019).
- Popov, D. et al. Real time study of grain enlargement in zirconium under room-temperature compression across the α to ω phase transition. *Sci. Rep.* **9**, 15712 (2019).
- Popov, D., Park, C., Kenney-Benson, C. & Shen, G. High pressure Laue diffraction and its application to study microstructural changes during the $\alpha \rightarrow \beta$ phase transition in Si. *Rev. Sci. Instrum.* **86**, 072204 (2015).
- Jamieson, J. C. Crystal structures at high pressures of metallic modifications of silicon and germanium. *Science* **139**, 762–764 (1963).
- Hu, J. Z., Merkle, L. D., Menoni, C. S. & Spain, I. L. Crystal data for high-pressure phases of silicon. *Phys. Rev. B* **34**, 4679 (1986).
- McMahon, M. I., Nelmes, R. J., Wright, N. G. & Allan, D. R. Pressure dependence of the Imma phase of silicon. *Phys. Rev. B* **50**, 739 (1994).
- Shen, G. et al. Direct observation of a pressure-induced precursor lattice in silicon. *Phys. Rev. Lett.* **109**, 205503 (2012).
- Katzke, H., Bismayer, U. & Tolédano, P. Theory of the high-pressure structural phase transitions in Si, Ge, Sn, and Pb. *Phys. Rev. B* **73**, 134105 (2006).
- Levitas, V. I., Chen, H. & Xiong, L. Lattice instability during phase transformations under multiaxial stress: Modified transformation work criterion. *Phys. Rev. B* **96**, 054118 (2017).
- Mizushima, K., Yip, S. & Kaxiras, E. Ideal crystal stability and pressure induced phase transition in silicon. *Phys. Rev. B* **50**, 14952 (1994).

13. Levitas, V. I., Chen, H. & Xiong, L. Triaxial-stress-induced homogeneous hysteresis-free first-order phase transformations with stable intermediate phases. *Phys. Rev. Lett.* **118**, 025701 (2017).
14. Olson, G. B. & Cohen, M. Dislocation theory of martensitic transformations. *Dislocations in Solids* 7th edn (ed. Nabarro, F. R. N., Elsevier Science Publishers BV) 297–407 (1986).
15. Stupkiewicz, S., Maciejewski, G. & Petryk, H. Low-energy morphology of the interface layer between austenite and twinned martensite. *Acta Mater.* **55**, 6292–6306 (2007).
16. Stupkiewicz, S., Maciejewski, G. & Petryk, H. Elastic micro-strain energy of austenite-martensite interface in NiTi. *Model. Simul. Mater. Sci. Eng.* **20**, 035001 (2012).
17. Bronstein, E., Faran, E. & Shilo, D. Analysis of austenite-martensite phase boundary and twinned microstructure in shape memory alloys: The role of twinning disconnections. *Acta Mater.* **164**, 520–529 (2019).
18. Levitas, V. I. Phase field approach for stress- and temperature-induced phase transformations that satisfies lattice instability conditions. Part 1. *Gen. theory Int. J. Plast.* **106**, 164–185 (2018).
19. Babaei, H. & Levitas, V. I. Phase field approach for stress- and temperature-induced phase transformations that satisfies lattice instability conditions. Part 2. Simulations of phase transformations Si I ↔ Si II. *Int. J. Plast.* **107**, 223–245 (2018).
20. Babaei, H. & Levitas, V. I. Finite-strain scale-free phase-field approach to multivariant martensitic phase transformations with stress-dependent effective thresholds. *J. Mech. Phys. Solids* **144**, 104114 (2020).
21. Steve, P. Fast parallel algorithms for short-range molecular dynamics. *J. Comput. Phys.* **117**, 1–19 (1995).
22. Balamane, H. Comparative study of silicon empirical interatomic potentials. *Phys. Rev. B* **46**, 2250 (1992).
23. Chang, J., Cai, W., Bulatov, V. V. & Yip, S. Molecular dynamics simulations of motion of edge and screw dislocations in a metal. *Comput. Mater. Sci.* **23**, 1–4 (2002).
24. Wang, G., Strachan, A., Cagin, T. & Goddard, W. A. III Molecular dynamics simulations of $1/2 \langle 111 \rangle$ screw dislocation in Ta. *Mater. Sci. Eng. A* **309**, 133–137 (2001).
25. Berendsen, H. J., Postma, J. V., Gunsteren, V., DiNola, W. F. & Haak, J. R. Molecular dynamics with coupling to an external bath. *J. Chem. Phys.* **81**, 3684 (1984).
26. <https://www.universitywafer.com/>. Si wafer parallel to (100), having thickness of $15 \pm 2 \mu\text{m}$.
27. Hirth, J. P. & Lothe, J. *Theory of dislocations* (Krieger Publishing Company, 1992).

Acknowledgements

H.C. acknowledges support by NSFC of China (52005186) and Shanghai Sailing Program (20YF1409400). V.I.L. work was sponsored by NSF (CMMI-1943710, MMN-1904830, and XSEDE TG-MSS170015), ONR (N00014-16-1-2079), and ISU (Vance Coffman Faculty Chair Professorship). DP and NV acknowledge High Pressure Collaborative Access

Team (HPCAT) (Sector 16), Advanced Photon Source (APS), Argonne National Laboratory. HPCAT operations are supported by DOE-NNSA's Office of Experimental Sciences. The Advanced Photon Source is a U.S. Department of Energy (DOE) Office of Science User Facility operated for the DOE Office of Science by Argonne National Laboratory under Contract No. DE-AC02-06CH11357. NV work is performed under the auspices of the U.S. Department of Energy by Lawrence Livermore National Laboratory under Contract DE-AC52-07NA27344.

Author contributions

H.C. performed computational and theoretical work. V.I.L. supervised computational and theoretical work and performed connection between theory and experiments. D.P. collected and analyzed X-ray diffraction data. V.L., D.P., H.C., and N.V. wrote the manuscript.

Competing interests

The authors declare no competing interests.

Additional information

Supplementary information The online version contains supplementary material available at <https://doi.org/10.1038/s41467-022-28604-1>.

Correspondence and requests for materials should be addressed to Valery I. Levitas or Dmitry Popov.

Peer review information *Nature Communications* thanks the anonymous reviewer(s) for their contribution to the peer review of this work. Peer reviewer reports are available.

Reprints and permission information is available at <http://www.nature.com/reprints>

Publisher's note Springer Nature remains neutral with regard to jurisdictional claims in published maps and institutional affiliations.



Open Access This article is licensed under a Creative Commons Attribution 4.0 International License, which permits use, sharing, adaptation, distribution and reproduction in any medium or format, as long as you give appropriate credit to the original author(s) and the source, provide a link to the Creative Commons license, and indicate if changes were made. The images or other third party material in this article are included in the article's Creative Commons license, unless indicated otherwise in a credit line to the material. If material is not included in the article's Creative Commons license and your intended use is not permitted by statutory regulation or exceeds the permitted use, you will need to obtain permission directly from the copyright holder. To view a copy of this license, visit <http://creativecommons.org/licenses/by/4.0/>.

© The Author(s) 2022

Supplementary material

Novel nanostructure, stress relaxation mechanisms, and crystallography for

pressure-induced Si-I \rightarrow Si-II phase transformation

Hao Chen¹, Valery I. Levitas^{2,3}, Dmitry Popov⁴, Nenad Velisavljevic⁵

¹ *Key Laboratory of Pressure Systems and Safety, Ministry of Education, School of Mechanical and Power Engineering, East China University of Science and Technology, Shanghai 200237, P.R. China*

² *Iowa State University, Departments of Aerospace Engineering and Mechanical Engineering, Ames, Iowa 50011, USA*

³ *Ames Laboratory, Division of Materials Science and Engineering, Ames, IA, USA*

⁴ *HPCAT, X-ray Science Division, Argonne National Laboratory, Lemont, Illinois, USA*

⁵ *HPCAT and Physics Division, Lawrence Livermore National Laboratory, Livermore, California 94550, USA*

Supplementary Note 1: Application of the traditional crystallographic theory

Transformation deformation gradients for three tetragonal variants of Si-II in a cubic coordinate are $\mathbf{F}_t^1 = \{a; a; b\}$, $\mathbf{F}_t^2 = \{a; b; a\}$, $\mathbf{F}_t^3 = \{b; a; a\}$, where $a = 1.175$ and $b = 0.553$ [1], i.e., transformation strains are very large, including large transformation volumetric strain $\det \mathbf{F}_t = -0.237$. Using the crystallographic theory of martensite [2], we obtain that all variants are in a twin relationship with (110) twinning plane and very large twinning shear $\gamma = 1.6548$. Compatibility condition for twinned Si-II – Si-I coherent interface with normal \mathbf{m} is

$$\mathbf{Q}' \cdot (\lambda \mathbf{Q} \cdot \mathbf{F}_t^2 + (1 - \lambda) \mathbf{F}_t^1) = \mathbf{I} + \mathbf{b} \otimes \mathbf{m} \quad (1)$$

where λ is the volume fraction of variant 2 in the two-variant mixture, \mathbf{Q} and \mathbf{Q}' are orthogonal tensors, \mathbf{I} is the unit tensor, and \mathbf{b} is a vector. The solution to Supplementary Eq. (1) is

$$\mathbf{m} = [0.3313 \quad -0.0961 \quad 0.3962]; \quad \mathbf{b} = [0.4099 \quad 0.2151 \quad -0.8864]; \quad \lambda=0.7386. \quad (2)$$

These results are far away from the results of MD simulations $\lambda=0.5$, $\mathbf{m} = [1; 1; 1]$, which shows that the traditional crystallographic theory is not applicable, in particular, due to large elastic strains.

Supplementary Note 2: Crystallographic theory for elastically deformed crystals

Actual deformation gradients for martensitic variants \mathbf{F}_1 , \mathbf{F}_2 , and \mathbf{F}_3 , and distorted Si-I \mathbf{F}_4 , as well as for Si-I matrix away from the interfaces \mathbf{F}_0 , with respect to unstressed Si-I, determined from MD simulations, in a coordinate system \mathbf{X} : $[110]$, \mathbf{Y} : $[\bar{1}10]$, \mathbf{Z} : $[001]$ are

$$\mathbf{F}_1 = \begin{bmatrix} 0.8998 & 0.5631 & 0.0133 \\ 0.0046 & 0.7145 & 0.0361 \\ 0.0027 & 0.0300 & 0.9769 \end{bmatrix}; \quad \mathbf{F}_2 = \begin{bmatrix} 0.9023 & -0.5982 & -0.0090 \\ -0.0641 & 0.7119 & 0.0126 \\ 0.0030 & -0.0698 & 0.9676 \end{bmatrix}; \quad (3)$$

$$\mathbf{F}_3 = \begin{bmatrix} 1.0187 & 0.0473 & -0.0023 \\ 0.0352 & 1.0538 & -0.1832 \\ -0.2028 & 0.2361 & 0.5124 \end{bmatrix}; \quad \mathbf{F}_4 = \begin{bmatrix} 0.7926 & 0.0154 & 0.1625 \\ 0.1069 & 1.0139 & -0.2713 \\ -0.2078 & 0.2393 & 0.8684 \end{bmatrix};$$

$$\mathbf{F}_0 = \begin{bmatrix} 0.9035 & 0 & 0 \\ 0 & 0.9035 & 0 \\ 0 & 0 & 0.9035 \end{bmatrix}. \quad (4)$$

The best way to take into account the elastic deformation of the austenite Si-I is to consider deformed Si-I as the new reference configuration. Then, relative deformation gradients are $\mathbf{F}_{i0} = \mathbf{F}_i \cdot \mathbf{F}_0^{-1}$, in particular,

$$\mathbf{F}_{10} = \begin{bmatrix} 0.9959 & 0.6232 & 0.0147 \\ 0.0051 & 0.7908 & 0.0400 \\ 0.0030 & 0.0332 & 1.0812 \end{bmatrix}; \quad \mathbf{F}_{20} = \begin{bmatrix} 0.9987 & -0.6621 & -0.010 \\ 0.071 & 0.7879 & 0.014 \\ 0.0033 & -0.0772 & 1.0709 \end{bmatrix}. \quad (5)$$

Compatibility conditions for coherent interfaces between twins and twinned Si-II and Si-I with the normals \mathbf{n} and \mathbf{m} are:

$$\mathbf{Q} \cdot \mathbf{F}_{20} - \mathbf{F}_{10} = \mathbf{a} \otimes \mathbf{n}; \quad \mathbf{Q}' \cdot (\lambda \mathbf{Q} \cdot \mathbf{F}_{20} + (1 - \lambda) \mathbf{F}_{10}) = \mathbf{I} + \mathbf{b} \otimes \mathbf{m}. \quad (6)$$

According to MD simulations, we use $\mathbf{n} = \{111\}$ and $\lambda=0.5$. Then the solution to Supplementary Eq. (6) is

$$\mathbf{m} = [-0.3370 \quad 0.2862 \quad -0.3899]; \quad \mathbf{b} = [-0.9050 \quad 0.1064 \quad 0.6937]. \quad (7)$$

The angle between \mathbf{m} and $[11\bar{1}]$ is 25.15° , which is quite large. This shows that even when elastic deformations of both Si-I and Si-II are taken into account, the traditional solution for twinned Si-II and Si-I interface is not an energy minimizer since MD simulations suggest a new, more sophisticated nanostructure.

Supplementary Note 3: Crystallographic analysis of the two-band nanostructure obtained in MD simulations

To determine deviation from the Hadamard compatibility conditions for bands I and II across $\{111\}$ interface, evaluated in terms of deformation gradients averaged of each band, we introduce the new Cartesian coordinate system, with axes 1 along $[111]$ direction, and mutually orthogonal axes 2 and 3 within $\{111\}$ interface. For example, we the following orthonormal vector basis

$$\mathbf{a}_1 = \left[\frac{1}{\sqrt{3}} \quad \frac{1}{\sqrt{3}} \quad \frac{1}{\sqrt{3}} \right]^T, \quad \mathbf{a}_2 = \left[-\frac{2}{\sqrt{6}} \quad \frac{1}{\sqrt{6}} \quad \frac{1}{\sqrt{6}} \right]^T, \quad \mathbf{a}_3 = \left[0 \quad \frac{1}{\sqrt{2}} \quad -\frac{1}{\sqrt{2}} \right]^T. \quad (8)$$

Then, the orthogonal matrix transforming the original coordinate system to Supplementary Eq. (8) is $\mathbf{R} = [\mathbf{a}_1 \quad \mathbf{a}_2 \quad \mathbf{a}_3]$. The deformation gradients matrices in the current coordinate system, $\mathbf{F}_{iR} = \mathbf{R} \cdot \mathbf{F}_i \cdot \mathbf{R}^T$, are as follows:

$$\begin{aligned}
\mathbf{F}_{1R} &= \begin{bmatrix} 0.5087 & 0.1769 & 0.2078 \\ -0.2188 & 1.0669 & 0.0583 \\ -0.1864 & 0.0705 & 1.0156 \end{bmatrix}; \quad \mathbf{F}_{2R} = \begin{bmatrix} 1.0876 & -0.0583 & -0.0363 \\ 0.3719 & 0.7281 & -0.2394 \\ 0.2889 & -0.2016 & 0.7660 \end{bmatrix}; \\
\mathbf{F}_{3R} &= \begin{bmatrix} 1.0032 & 0.0877 & -0.1220 \\ -0.2448 & 0.7223 & 0.3177 \\ 0.1934 & 0.2393 & 0.8594 \end{bmatrix}; \quad \mathbf{F}_{4R} = \begin{bmatrix} 0.8825 & 0.1025 & -0.3435 \\ -0.2789 & 0.8685 & 0.0240 \\ 0.1671 & 0.0316 & 0.9239 \end{bmatrix}, \quad (9)
\end{aligned}$$

while \mathbf{F}_0 does not change. Averaged over bands I, II and I+II deformation gradients are

$$\begin{aligned}
\mathbf{F}^I &= c_1 \mathbf{F}_{1R} + c_2 \mathbf{F}_{2R} = \begin{bmatrix} 0.7981 & 0.0593 & 0.0857 \\ 0.0765 & 0.8975 & -0.0905 \\ 0.0513 & -0.0656 & 0.8908 \end{bmatrix}; \quad \det \mathbf{F}^I = 0.6246; \\
\mathbf{F}^{II} &= c_3 \mathbf{F}_{3R} + c_4 \mathbf{F}_{4R} = \begin{bmatrix} 0.9558 & 0.0935 & -0.2090 \\ -0.2582 & 0.7798 & 0.2023 \\ 0.1831 & 0.1577 & 0.8847 \end{bmatrix}; \quad \det \mathbf{F}^{II} = 0.6921; \\
\mathbf{F}^{av} &= \lambda_1 \mathbf{F}_{1R} + \lambda_2 \mathbf{F}_{2R} + \lambda_3 \mathbf{F}_{3R} + \lambda_4 \mathbf{F}_{4R} = \begin{bmatrix} 0.8712 & 0.0712 & 0.0043 \\ -0.0167 & 0.8952 & -0.0098 \\ 0.0908 & -0.0039 & 0.9203 \end{bmatrix};
\end{aligned}$$

$$\det \mathbf{F}^{av} = 0.718, \quad (10)$$

with

$$c_1 = 0.5, c_2 = 0.5; c_3 = 0.6071, c_4 = 0.3929;$$

$$\lambda_1 = 0.3742, \lambda_2 = 0.3742, \lambda_3 = 0.1740, \lambda_4 = 0.1126.$$

Also, $\det \mathbf{F}_0 = 0.763$.

Let us evaluate jump in deformation gradient at different interfaces:

$$\mathbf{F}^I - \mathbf{F}_0 = \begin{bmatrix} -0.1054 & 0.0593 & 0.0857 \\ 0.0765 & -0.0060 & -0.0905 \\ 0.0513 & -0.0656 & -0.0127 \end{bmatrix};$$

$$\begin{aligned}
\mathbf{F}^{II} - \mathbf{F}_0 &= \begin{bmatrix} 0.0523 & 0.0935 & -0.2090 \\ -0.2582 & -0.1237 & 0.2023 \\ 0.1831 & 0.1577 & -0.0188 \end{bmatrix}; \\
\mathbf{F}^{av} - \mathbf{F}_0 &= \begin{bmatrix} -0.0323 & 0.0712 & 0.0043 \\ -0.0167 & -0.0083 & -0.0098 \\ 0.0908 & -0.0039 & 0.0168 \end{bmatrix}; \\
\mathbf{F}^{II} - \mathbf{F}^I &= \begin{bmatrix} -0.1576 & -0.0342 & 0.2948 \\ 0.3348 & 0.1177 & -0.2928 \\ -0.1318 & -0.2232 & 0.0061 \end{bmatrix}. \tag{11}
\end{aligned}$$

Five components of these matrices located in the first row and column characterize strains normal to $\{111\}$ interface, which do not participate in the Hadamard compatibility conditions. The remaining 2×2 minors of these matrices describe interface distortion:

$$\begin{aligned}
\mathbf{F}'_{||} - \mathbf{F}_{0||} &= \begin{bmatrix} -0.0060 & -0.0905 \\ -0.0656 & -0.0127 \end{bmatrix}; \\
\mathbf{F}''_{||} - \mathbf{F}_{0||} &= \begin{bmatrix} -0.1237 & 0.2023 \\ 0.1577 & -0.0188 \end{bmatrix}; \\
\mathbf{F}^{av} - \mathbf{F}_{0||} &= \begin{bmatrix} -0.0083 & -0.0098 \\ -0.0039 & 0.0168 \end{bmatrix}; \\
\mathbf{F}''_{||} - \mathbf{F}'_{||} &= \begin{bmatrix} 0.1177 & -0.2928 \\ -0.2232 & 0.0061 \end{bmatrix}. \tag{12}
\end{aligned}$$

For compatible interfaces that satisfy the Hadamard compatibility conditions, all matrices in Supplementary Eq. (12) are equal to zero. Since distortions are finite, to separate rotations and stretches, we

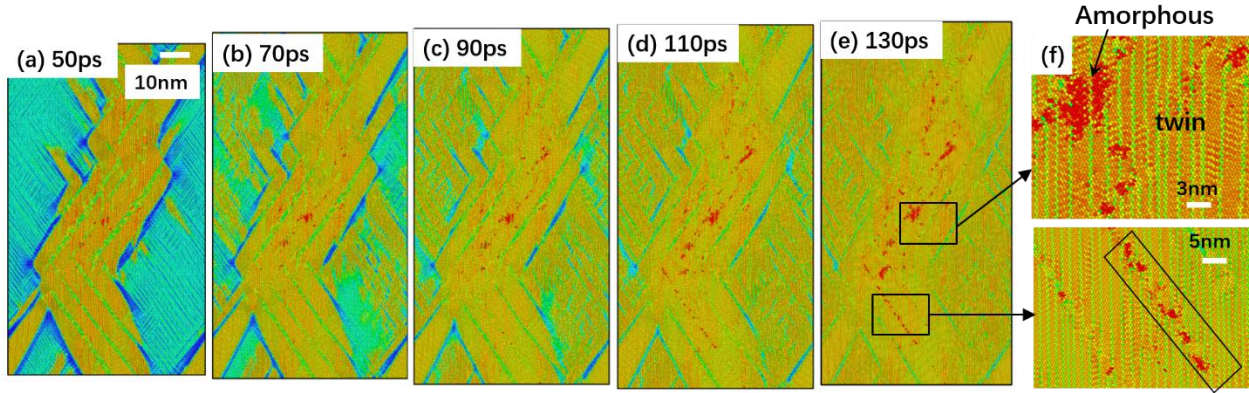
- (a) add to all of them \mathbf{I} , transforming them to deformation gradient at the interface \mathbf{F}_{int} ,

(b) calculate the corresponding right stretch tensor $\mathbf{U}_{\text{int}} = (\mathbf{F}_{\text{int}}^T \cdot \mathbf{F}_{\text{int}})^{0.5}$,

(c) calculate the strain tensor $\mathbf{U}_{\text{int}} - \mathbf{I}$ and its two-principle value, which we will call incompatibility \mathbf{Inc} .

Thus, for the band I-Si-I interface, $\mathbf{Inc} = (0.069; 0.087)$, i.e., corresponding strains are finite, which along with local stresses due to alternating twin tips cause nucleation of the band II. For the band II-Si-I interface, $\mathbf{Inc} = (0.117; 0.258)$, which causes much higher local stresses. For the band I-band II interface, $\mathbf{Inc} = (0.326; 0.201)$, which leads to huge local stresses. All these interfacial stresses are short-range and partially relax by local atomic rearrangements and loss of coherence; see interfaces in Fig. 2b. However, averaged over the band I and band II deformation gradient \mathbf{F}_{av} produces with Si-I very small incompatibility $\mathbf{Inc} = (0.004; 0.021)$. In addition, normal to the $\{111\}$ interface strain for bands I + II with respect to Si-I is also very small (-0.032) and difference in volumetric deformation gradients $\det \mathbf{F}_{\text{av}} - \det \mathbf{F}_0 = -0.045$, i.e., very small as well. All these facts produce almost self-accommodated band I + band II microstructure with small strain within Si-I matrix, and consequently, small long-range internal stresses.

Supplementary Note 4: The later stages of the evolution of Si-II structure under high pressure



Supplementary Figure 1 The later evolution of the microstructure growing from two dislocation-induced nuclei. Bands II (green) gradually disappear during the evolution (a-e), and the final microstructure consists of twinned Si-II variants with deformation gradients \mathbf{F}_1 and \mathbf{F}_2 , separated by (110) twinning plane (f). Twinned bands nucleated from different dislocation sites meet with each other and form an intermediate amorphous phase (f).

The initial evolution of Si-II exhibiting the nontrivial two-band structure is shown in Fig. 3 in the main text. The later evolution of the microstructure is shown in Supplementary Figure 1. With reducing volume fraction of remaining Si-I matrix and the elastic constraint due to the matrix, the width of band II (green region) and the volume fraction λ_3 of the variant \mathbf{F}_3 reduce. After Si-I matrix disappeared, band II disappears as well, leaving twinned Si-II and relaxing elastic stresses. Significant relaxation of lattice distortions in Si-II after completing PT was observed with XRD as well, indicated by “streaky” Laue and arch-like monochromatic beam reflections (Fig. 2). The final stable structure is a twinned structure consisted of \mathbf{F}_1 and \mathbf{F}_2 , which corresponds to experiments (Fig. 2). Different twinned bands I nucleated from different dislocation sites can meet each other during evolution. When the twins match each other, perfect coalescence occurs, as

shown in Supplementary Figure 1(f). However, if they do not match each other, an intermediate amorphous phase is formed (Supplementary Figure 1).

We need to mention some discrepancies between MD simulation and experiment related, most probably to dislocational relaxation of internal stresses in experiment and absence of dislocation activity in MD simulations, due to chosen interatomic potential and smaller time and space scales. Thus, large elastic distortions from cubic Si-I and tetragonal Si-II observed in MD, relaxed in the experiment due to dislocation activity and arrest the nanostructure of the type shown in Fig. 3, leaving significant misorientation of different domains of Si-II. In contrast, in MD simulations, after completing PT, intermediate bands and misorientation disappear, leaving almost perfect twinned structure (Supplementary Figure 1).

Supplementary Note 5: High-pressure Laue diffraction

Supplementary Note 5.1: Experimental details and data analysis

The Si sample was put into a diamond anvil cell (DAC) with culets having 500 μm diameters using a micromanipulator [3]. Re gasket was pre-indented down to 60 μm and, after that, a hole of 300 μm diameter was drilled in the gasket with a laser drilling machine [4]. The DAC was loaded by He as a pressure transmitting medium. While it is mentioned in [5] that He penetrates into SiO₂ glass and essentially changes its compressibility and is detected in Raman spectra, we did not find any mentioning of such effects for Si-I in the huge existing literature. Even in [5], neither GeO₂ glass nor crystalline phases of SiO₂ demonstrated this phenomenon.

Since pressure for Si-I to Si-II PT is well known and PT occurs at about 13 GPa ([3,6-10], we did not focus on precise detection of PT pressure in this study and did not use online Ruby fluorescence system to monitor pressure. The pressure was increased to approach the PT with the membrane system while measuring pressure using the off-line Ruby fluorescence system [11], available in

the experimental hutch. At 12.3 GPa, the DAC was mounted on the setup, and membrane pressure was further increased remotely in small steps, simultaneously collecting series of 2D scans. After each step of pressure increase, microstructural changes of the sample were watched in real time with ImageJ software [12]. Only if no notable changes were observed during multiple 2D scans was pressure increased by another step. After about 14 hours, the first changes in the sample due to the PT transition were observed, and membrane pressure was not increased any more. The transition was mainly completed in 38 minutes, although a small piece of the initial Si-I sample existed even more than 4 hours after the transition in the other parts of the studied area was finished (see below). The pressure was measured again with the Ruby system, 22 hours after the data collection procedure started, and found to be 13.8 GPa. Therefore, the pressure rate was less than 0.1 GPa/hour in average; although it was higher before the transition (as membrane pressure was increased) and, most likely, pressure still slightly increased also after the transition (as typically DACs have some pressure drifts even without an increase of membrane pressure). Note that the current pressure controlling system cannot control pressure with better precision than a few kbar/hour. Thus, PT occurred at ~13 GPa, and the estimated pressure increase during 38 minutes between initiation and completion of PT should not exceed 0.1 GPa. The pressure range and pressure rate here are like that in [3,6] (0.2-0.3 GPa/hour); thus, combining results from both experiments is legitimate.

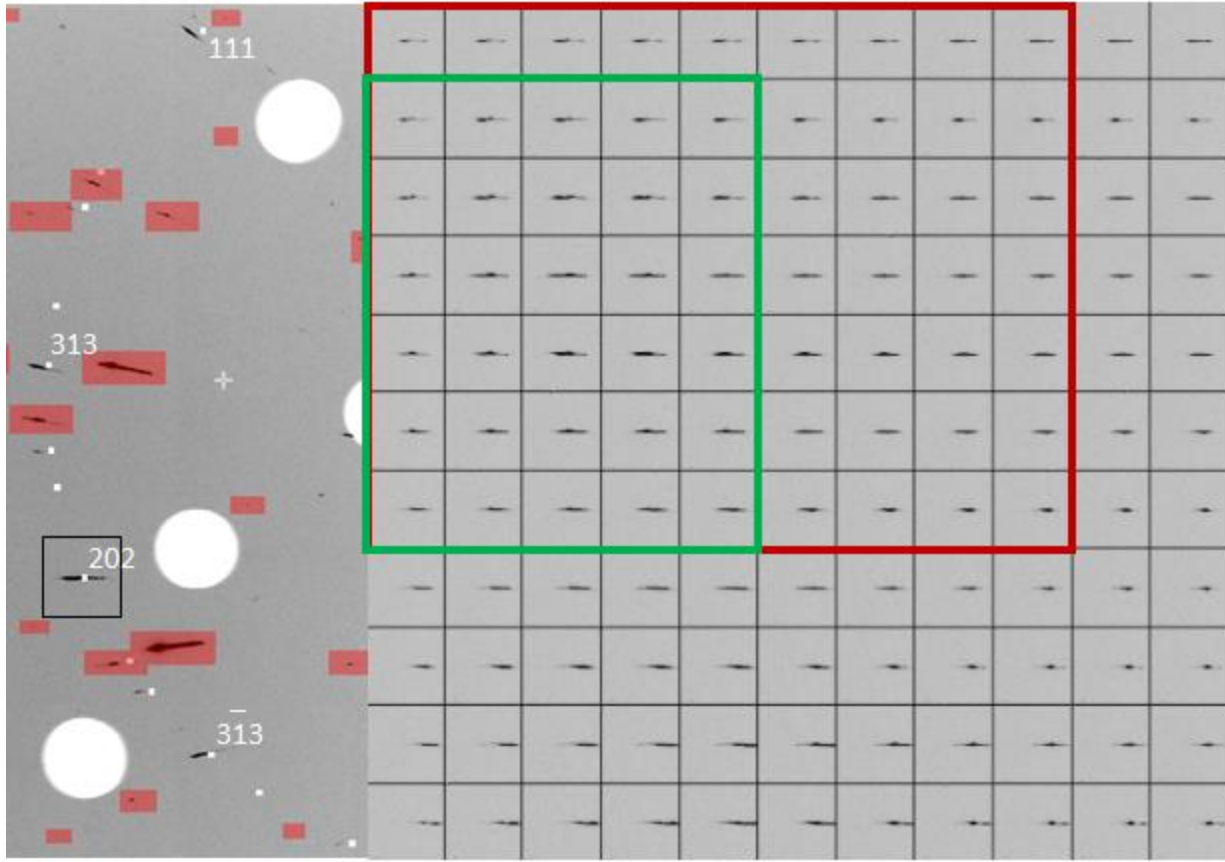
As the sample position may slightly shift due to increased pressure, the sample was periodically re-centered on the rotation axis by doing absorption scans with a photodiode to keep the sample at the same position with respect to the X-ray beam and area detector [13,14]. No re-centering was done after alterations of the sample started, but after the data collection was finished, sample position with respect to the beam was re-determined, and shift of the sample relative to the

previously determined position was less than 1 μm . This indicates that all the 2D scans were collected on the same area of the sample across the transition.

The data analysis procedure consisted of two steps [3]. Laue reflections from the sample were indexed first in order to identify crystals and find their orientations. After that, maps of reflections have been generated to detect changes of crystal morphology and deformation of the crystals due to the transition. Indexation and mapping of reflections were done with software polyLaue developed in-house by D. Popov [3]. Diffraction patterns have been visualized with the Dioptas program [15,16]. Maps of reflections have been visualized with the Fit2d program [17,18]. The strongest reflections from diamonds may damage the area detector. Therefore, such reflections were blocked by a detector mask [3]. All other reflections from diamonds have been identified by indexation and excluded from further data analysis.

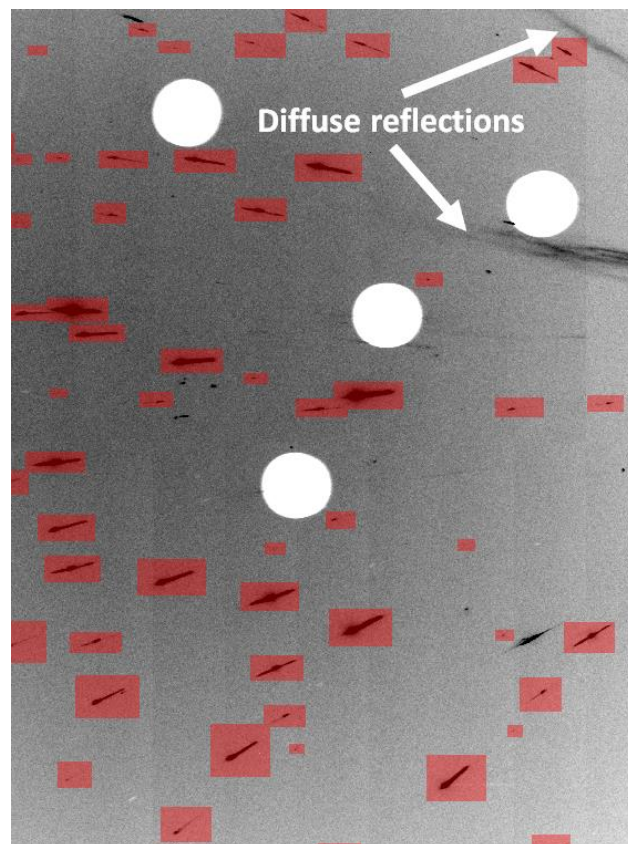
Supplementary Note 5.2: Results and discussion

A typical diffraction pattern and map of a reflection right on the onset of the transition are presented in Supplementary Figure 2. The numbering of all other 2D scans considered below starts from this scan. During the first five 2D scans, starting from the onset, the sample exhibited severe deformation. Positions of reflections substantially varied across the sample, indicating variation of crystal orientation. At the same time, crystal morphology also changed because some parts of the sample transformed to Si-II. All the maps of reflections obtained during scans 1-5 were very different from each other, even if they were obtained from adjacent scans because sample alterations took shorter periods of time than required to collect one 2D scan. Therefore, changes of the sample during scans 1-5 could not be identified.



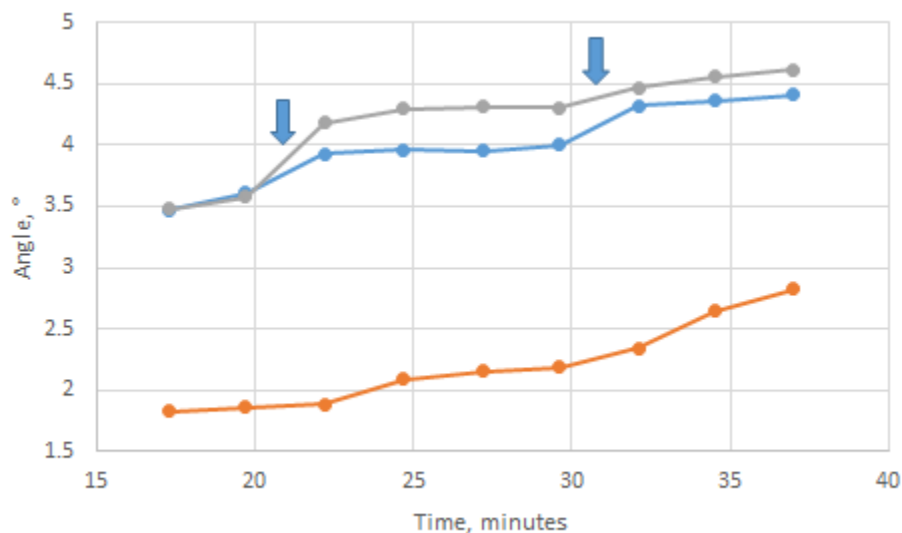
Supplementary Figure 2 Laue diffraction pattern (left) and map of 202 reflection (right) from Si-I obtained right on the onset of the $\alpha \rightarrow \beta$ transition. Predicted positions of reflections, assuming the highest X-ray energy limit of 80keV and d-values of reflections larger than 0.5\AA , are shown on the diffraction pattern as white rectangles slightly shifted to the right not to overlap with the observed reflections. Black rectangle in the diffraction image denotes an area used to build the composite frame in the right. The step size of the translational scan was $1\ \mu\text{m}$. The numbering and time intervals of the scans mentioned in the Supplementary materials, movies and other figures start from the scan presented in this figure. Areas within red and green boxes are occupied by the Si-I crystals referenced in the Supplementary materials as crystals 1 and 2, respectively. These areas are presented in Supplementary movies 1-4. Reflections from diamonds on the Laue pattern are denoted by red transparent rectangles. White circles on the Laue image are due to the detector mask.

Starting from 2D scan 6, only a few pieces of the original Si-I sample remained in the studied area. Still, these crystals were stable enough to produce maps of reflections reproducible during multiple 2D scans, and, therefore, it was possible to identify these crystals. Maps of reflections and diffraction patterns, obtained during multiple 2D scans from two of these crystals, were combined in the same order as these maps, and diffraction patterns were obtained (Supplementary movies 1-4). These crystals are referenced below as crystal 1 (Supplementary movies 1 and 2, area outlined in red in Supplementary Figure 2) and crystal 2 (Supplementary movies 3 and 4, area outlined in green in Supplementary Figure 2).



Supplementary Figure 3 Diffuse reflections from Si-II. White circles are due to the detector mask. Red rectangles denote reflections from diamonds.

After the onset of the transition, very diffuse reflections from the high-pressure phase were observed (Supplementary Figure 3). ‘Streaky’ shape of these reflections indicated that the product Si-II phase exhibited strong misorientation of its nanodomains. This observation agrees with the previous results [3,6]. Indexation of reflections from Si-II was impossible.

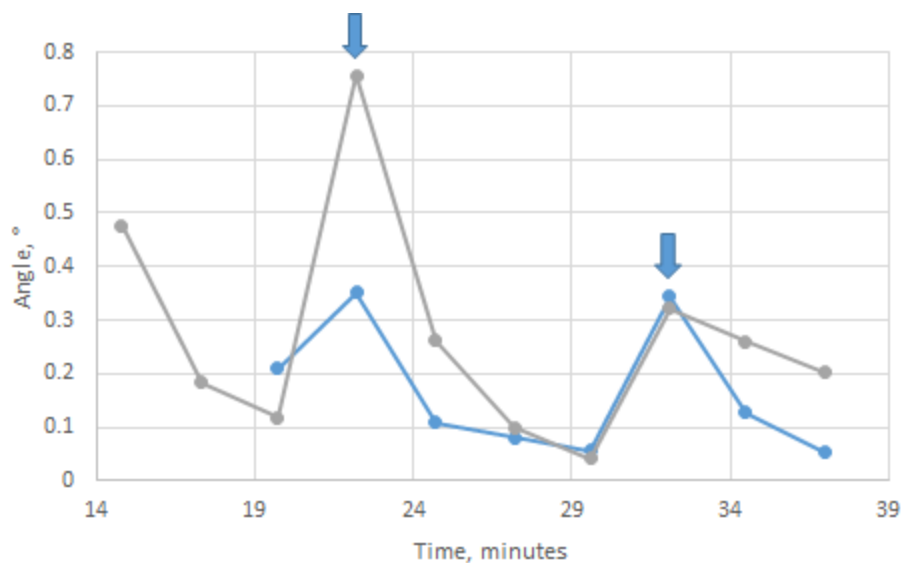


Supplementary Figure 4 Angular deviations versus time of Si-I crystals, referenced in the Supplementary materials as crystals 1 (gray) and 2 (blue), from the parental Si-I crystal at the onset of the $\alpha \rightarrow \beta$ transition. These deviations may include rigid-body rotation of the entire sample due to a change in its shape. Angles between crystals 1 and 2 versus time (yellow). Vertical arrows denote time points when crystal 1 exhibited a much faster decrease of its size than on average. Time starts from the scan presented in Supplementary Figure 2.

Due to the deformation process, orientations of crystals 1 and 2 were shifted by about 3.5° with respect to the sample orientation, which was observed right on the onset of transition. Orientations of crystals 1 and 2 were also shifted with respect to one another by about 1.8° . Absolute and relative angular deviations of crystals 1 and 2 gradually increased further across the transition (Supplementary Figure 4). In about 20 minutes, absolute and relative angular shifts

reached about 4.5° and 2.8° , respectively. Strong deformation of the sample right after the onset of the transition and relative angular shifts of crystals 1 and 2 are caused by heterogeneous internal stresses due to transformation strain in Si- II phase. Interaction of the sample with pressure medium, diamond, and gasket mainly contributes to the absolute angular shifts due to rigid-body rotation of the entire sample but essentially does not affect relative angular shifts of crystals 1 and 2.

Results from crystal 1 indicate that the speed of the transition can be fundamentally faster comparing to what can be concluded based on the total time of transition. Starting from 2D scan 6, crystal 1 existed for about 26 minutes before it was completely transformed to Si-II. However, mostly, the transformation took place in two short periods of time, less than a minute each, between scans 9 and 10 and between scans 13 and 14 (Supplementary movies 1,2). Interestingly, during these two periods of time, both crystals 1 and 2 exhibited shifts of their absolute orientations notably higher than on average while their relative orientation changed as normal (Supplementary Figure 4 and 5). This is the indication that these two periods of time, when the transition was fundamentally faster than in average, were accompanied by substantial changes of orientation of the entire sample or, if the sample was fragmented (broken) to smaller pieces because of the deformation, by reorientation of the pieces of the sample containing crystals 1 and 2 as a whole.

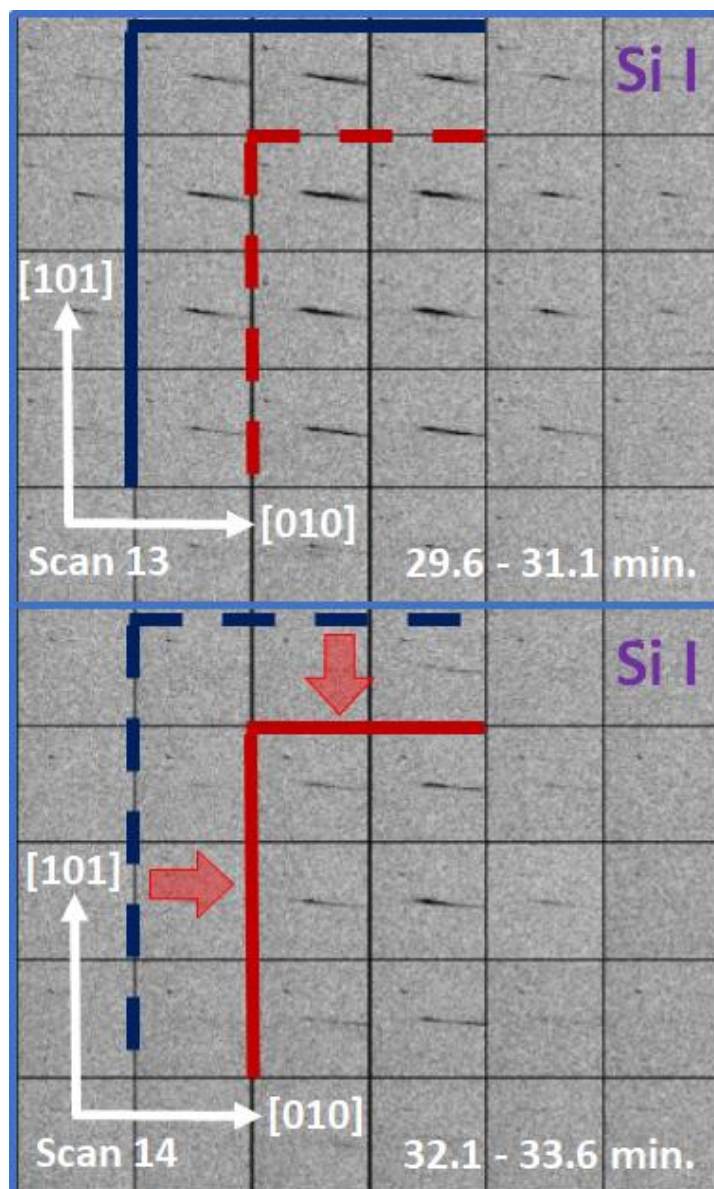


Supplementary Figure 5 Angular shifts between adjacent scans versus time for Si-I crystals, referenced in the Supplementary materials as crystals 1 (gray) and 2 (blue), across the $\alpha \rightarrow \beta$ transition in Si. Vertical arrows denote time points when crystal 1 exhibited a much faster decrease of its size than on average. Time starts from the scan presented in Supplementary Figure 2.

Variations of the transition speed can be explained by the known fact that the speed of transition is substantially controlled by crystal lattice defects (not included in the simulations), introducing activation barriers. Due to heterogeneity of the defects distribution, interface propagation rate may vary significantly. After waiting for a long time near an obstacle with high activation barrier and then overcoming it with the help of strong thermal fluctuation, some portion of the interface may travel fast for a relatively large distance until it meets the next strong barrier. At the same time, crystal 2 does not exhibit any notable acceleration of the transition simultaneously with crystal 1 (Supplementary movies 1-4). This indicates that crystal lattice defects, individual for each of the crystals, are the major factor defining the speed of transition. Starting from 2D scan number 16, after 38 minutes from the first 2D scan, no Laue reflections from Si-I except those from crystal 2 were observed on the studied area of the sample. Crystal 2

was not transformed to Si-II phase even 4 hours 2 minutes after scan 16, when Laue diffraction measurements were finished (Supplementary movies 3, 4). This agrees with the defect-controlled transformation speed and thermally activated mechanism of the interface motion.

Crystals of Si-I, coexisting with Si-II, may exhibit changes in their deformation state, which agrees with the previous results [3,6]. A possible explanation of these changes is essentially the same as for the reorientations of Si-I crystals across the transition. For instance, crystal 2 produced sharper reflections starting from 2D scan 10, compared to the previous scans, indicating a relaxation process. When the transition was almost finished in the studied area and only crystal 2 coexisted with the high-pressure phase, crystal 2 exhibited quite notable changes in its deformation state. Reflection 111 became much more broaden comparing to $1\bar{1}1$. One possible explanation of this observation is that crystal 2 may become slightly bent cylindrically around a direction close to $1\bar{1}1$ [19]. Similar lattice rotation of Si-I crystals coexisting with Si-II has been reported previously [3,6].



Supplementary Figure 6 Shifts of the Si-I / Si-II interfaces (denoted by red arrows), projected onto a $\{110\}$ plane of the Si-I crystal referenced as crystal 1 in the Supplementary materials. Shifts of the Si-I / Si-II interfaces are detected from maps of 202 reflection. The intensity scaling of both maps is kept the same before and after the shift as defined in Fit2d program [17,18]. The interfaces before and after their shifts are denoted by dark blue and red lines, respectively; solid lines denote currently existing interfaces, and dashed lines denote interfaces existing in different states. The numbering and time intervals of the scans start from the scan presented in Supplementary Figure 1.

Maps of crystals 1 and 2, obtained in real-time, provide information on the orientation of the Si-I / Si-II interface as projected onto the {110} plane approximately perpendicular to the incident beam. Edges of crystals 1 and 2, projected onto the {110} plane, are oriented about parallel to one of the following directions $\langle 111 \rangle$, $\langle 110 \rangle$ or $\langle 100 \rangle$ (Supplementary movies 1-4). However, this criterion for the interface is not reliable because the edges of the crystals may have been formed by cracking the original sample due to the deformation process and not by the interface. Much more reliable way to detect the interface between parental and product phases is the observation of shifts of the parental phase edges across the transition. Crystal 1 exhibited very notable shifts of the Si-I / Si-II interface, detected this way, between scans 9 and 10 (Supplementary movies 1, 2) and between scans 13 and 14 (Supplementary Figure 6 and movies 1 and 2). These shifts indicate interfaces parallel to $\langle 110 \rangle$ and $\langle 100 \rangle$.

Experiments also reveal that: (a) this PT is rather nucleation controlled because after nucleation it proceeds until completing at the same pressure; (b) kinetics is thermally activated, with two burst-like fast transformation increments and slow transformation otherwise; (c) speed of transition is controlled by kinetic factors not included into the simulations. These factors are defined by defects of the original Si-I single-crystal because the speed of the PT is quite different in different regions of crystals.

Supplementary Note 6: Reconstructive versus martensitic phase transformation from Si-I to Si-II

The potential problem often arises from the different classifications of structural PTs in different communities. One of the communities, which focuses on bonding between atoms, calls PT a reconstructive if it involves breaking/changing the bonds; see the book [20]. Alternative PTs without bond breaking are often called displacive. Then the PT from the semiconductive Si-I to

metallic Si-II clearly belongs to reconstructive PTs [20-23]. There are some other features of these groups of PTs, e.g., reconstructive PT involves large displacements, and no group-subgroup relationship exists between phases, while for displacive PTs, displacements are small, and phases obey group-subgroup relationship [20]. Communities that are concerned with material science, crystallographic, and microstructural aspects do not care about bonding and divide structural PTs into diffusive and diffusionless or martensitic [2,24-27]. Diffusive PTs are accompanied by diffusion and exchange of atomic neighbors during PT, like amorphization and PT occurring via intermediate disordered/amorphous state, precipitation, eutectoid, and massive PT, as well as ordering. Martensitic PTs, in contrast, do not involve diffusion and exchange of atomic neighbors, and mapping of positions of two lattices can be presented by homogeneous deformation (transformation deformation gradient) and some additional intra-cell displacements called shuffles or shifts. Twinning is considered a particular case of martensitic PT, for which the same lattices are connected by a transformation deformation gradient representing simple shear along the twinning plane. Internal stresses and evolution of martensitic microstructure are determined by minimization of the elastic energy, which, in addition to an external load, is completely determined by the field of the transformation deformation gradient and is independent of shuffles. That is why the main parameter in the crystallographic theory and theory of the microstructure is the transformation deformation gradient [2,27], independent of breaking or not breaking bonds. These theories determine, based on the transformation deformation gradient and assumed mode of the lattice-invariant shear (slip or twinning), normal to the habit and twinning planes, the volume fraction of twin-related martensitic variants (see Supplementary Eqs. (1)-(2)), and orientation relationship between lattices of different phases [2,27].

Most of the reconstructive PTs discussed in the monograph [20] are described by the crystallographic theory of martensitic PTs, including PT in iron [27], shape memory alloys [2], plutonium [28], and hexagonal and rhombohedral graphite to hexagonal and cubic diamond and similar PTs in BN [29,30]. It is mentioned in [30] that graphite-like phases of BN have very strong covalent bonds with sp^2 hybridization within the hexagonal planes and weak van der Waals bonds between these planes, while cubic or wurtzitic superhard BN have only covalent (partially ionic) bonds, with tetrahedral three-dimensional sp^3 hybridization; the same is true for graphite and diamond. Despite the reconstructive PT between these phases, all aspects of crystallographic and microstructure formation theory are applied in [29,30] to these PTs; they are called martensitic in [29].

With a full understanding of change in bonding during PT Si-I – Si-II in [1,31], it is treated as martensitic PT in which the transformation deformation gradient connects atoms of Si-I and Si-II lattice even without shuffles. All continuum theories of PTs involving the transformation deformation gradient (e.g., based on energy minimization [2] or phase field theories [32-31], including those for Si [32-34]) do not distinguish bonding. However, some works distinguish between reconstructive martensitic PTs, for which no group-subgroup relationship exists between phases, and “weak” martensitic PTs, for which phases obey group-subgroup relationship [35,36]. Reconstructive martensitic PTs are more complex for modeling because the reverse PT may occur to different variants of the austenite related by a lattice-invariant shear. But this is not the case for cubic to tetragonal PT Si-I – Si-II.

To summarize, various definitions of martensitic and reconstructive PTs are used by different research communities depending on their goals. For example, the firefighters distinguish a violin from a piano in a simple way: the piano burns longer, which is sufficient for their goals.

Since our main goal here is crystallography and microstructure rather than atomic bonding, we call Si-I to Si-II PT martensitic. Our results and conclusions would not change if we called them reconstructive or by any other name.

Supplementary References:

1. Zarkevich, N.A., Chen, H., Levitas, V.I. and Johnson, D.D., 2018. Lattice instability during solid-solid structural transformations under a general applied stress tensor: Example of Si-I \rightarrow Si-II with metallization. *Phys. Rev. Lett.* 121(16), p.165701.
2. Bhattacharya, K., 2003. Microstructure of Martensite. Why it Forms and How It Gives Rise to the Shape-Memory Effect. Oxford University Press.
3. Popov, D.; Velisavljevic, N. and Somayazulu, M. (2019) Mechanisms of Pressure-Induced Phase Transitions by Real-Time Laue Diffraction. *Crystals* 9, 672
4. Hrubiak, R.; Sinogeikin, S.; Rod, E.; Shen, G. The laser micro-machining system for diamond anvil cell experiments and general precision machining applications at the High Pressure Collaborative Access Team. *Rev. Sci. Instrum.* **86**, 072202 (2015).
5. Shen, G.; Mei, Q.; Prakapenka, V.; Lazor, P.; Sinogeikin, S.; Meng, Y. and Park C. Effect of helium on structure and compression behavior of SiO₂ glass. *PNAS* **108**, 6004-6007 (2011).
6. Popov, D., Park, C., Kenney-Benson, C. & Shen, G. High pressure Laue diffraction and its application to study microstructural changes during the $\alpha \rightarrow \beta$ phase transition in Si. *Rev. Sci. Instrum.* 86, 072204 (2015).
7. Jamieson, J. C. Crystal structures at high pressures of metallic modifications of silicon and germanium. *Science* 139, 762-4 (1963).
8. Hu, J. Z., Merkle, L. D., Menoni, C. S. & Spain, I. L. Crystal data for high-pressure phases of silicon. *Phys. Rev. B* 34, 4679 (1986).
9. McMahon, M. I., Nelmes, R. J., Wright, N. G., and Allan, D. R., Pressure dependence of the Imma phase of silicon. *Phys. Rev. B* 50(2), 739 (1994).

10. Shen, G., Ikuta, D., Sinogeikin, S., Li, Q., Zhang, Y., and Chen, C., Direct Observation of a Pressure-Induced Precursor Lattice in Silicon. *Phys. Rev. Lett.* 109, 205503 (2012).
11. Mao, H.K.; Xu, J.; Bell, P.M. Calibration of the Ruby pressure gauge to 800-kbar under quasi-hydrostatic conditions. *J. Geophys. Res.: Solid Earth* **1986**, *91*, 4673-4676
12. <https://imagej.nih.gov/ij/>
13. Smith, J.S.; Desgreniers, S. Selected techniques in diamond anvil cell crystallography: centring samples using X-ray transmission and rocking powder samples to improve X-ray diffraction image quality. *J. Synchrotron Radiat.* **2009**, *16*, 83–96
14. Smith, J.S.; Rod, E.A.; Shen G. Fly scan apparatus for high pressure research using diamond anvil cells. *Rev. Sci. Instrum.* **2019**, *90*, 015116
15. Prescher, C.; Prakapenka, V. DIOPTAS: a program for reduction of two-dimensional X-ray diffraction data and data exploration. *High Pressure Res.* **2015**, *35*, 223–230
16. <http://www.clemensprescher.com/programs/dioptas>
17. Hammersley, A. P.; Svensson, S. O.; Hanfland, M.; Fitch, A. N.; Hausermann, D. Two-dimensional detector software: from real detector to idealized image or two-theta scan. *High Pressure Res.* **1996**, *14*, 235-248
18. <http://www.esrf.eu/computing/scientific/FIT2D/>
19. Yang W., Larson B. C., Ice G. E., Tischler J. Z., Budai J. D., and Chung K.-S. Spatially resolved Poisson strain and anticlastic curvature measurements in Si under large deflection bending. *Applied Physics Letters* **2003**, *82*(22), 3856
20. P. Toledano and V. Dmitriev, *Reconstructive Phase Transitions*, (World Scientific, New Jersey, 1996).

21. A. Mujica, A. Rubio, A. Munoz, and R. J. Needs. High-pressure phases of group-IV, III–V, and II–VI compounds. *Rev. Mod. Phys.* 75, 863 (2003)
22. L. Q. Huston, A. Lugstein, J. S. Williams, and J. E. Bradby. The high pressure phase transformation behavior of silicon nanowires. *APL* 113, 123103 (2018)
23. E. E. McBride, A. Krygier, A. Ehnes, E. Galtier, M. Harmand, Z. Konôpková, H. J. Lee, H.-P. Liermann, B. Nagler, A. Pelka, M. Rödel, A. Schropp, R. F. Smith, C. Spindloe, D. Swift, F. Tavella, S. Toleikis, T. Tschentscher, J. S. Wark and A. Higginbotham. Phase transition lowering in dynamically compressed silicon. *Nature Phys* 15, 89–94 (2019)
24. Porter D, Easterling K. Phase transformation in metals and alloys. New York: Van Nostrand Reinhold; 1992.
25. Fultz B. Phase transitions in materials. Cambridge University Press, Cambridge, 2014.
26. J. Christian, G. Olson, M. Cohen. Classification of Displacive Transformations: What is a Martensitic Transformation? *J. de Physique IV, Colloque C8, supplement au J. de Physique III*, 1995, 5, pp. 3-10.
27. Wayman, C.M., 1964. Introduction to the Crystallography of Martensitic Transformation. New York, Macmillan.
28. Adler, P., Olson, G., Stevens, M., and Gallegos, G., 1992. On the Constitutive Relations for δ - α and α - δ Martensitic-Transformation Plasticity in Plutonium Alloys. *Acta Metall. Mater* 40, 1073-1082.
29. V. F. Britun and A. V. Kurdyumov. Analysis of the effect of nonhydrostatic compression conditions on direct phase transformations in carbon. *Powder Metallurgy and Metal Ceramics*, 41, 7-8, 2002.

30. L. C. Nistor , G. Van Tendeloo & G. Dinca (2005) Crystallographic aspects related to the high pressure–high temperature phase transformation of boron nitride, *Philosophical Magazine*, 85, 1145-1158.
31. Malyushitskaya, Z.V., 1999. Mechanisms Responsible for the Strain-Induced Formation of Metastable High-Pressure Si, Ge, and GaSb Phases with Distorted Tetrahedral Coordination. *Inorganic Materials* 35, 425-430.
32. Levitas, V. I. Phase field approach for stress- and temperature-induced phase transformations that satisfies lattice instability conditions. Part 1. General theory. *Int. J. Plast.* 106, 164-185 (2018).
33. Babaei, H. & Levitas, V. I. Phase field approach for stress- and temperature-induced phase transformations that satisfies lattice instability conditions. Part 2. Simulations of phase transformations Si-I \leftrightarrow Si-II. *Int. J. Plast.* 107, 223-245 (2018).
34. Babaei, H. & Levitas V. I. Finite-strain scale-free phase-field approach to multivariant martensitic phase transformations with stress-dependent effective thresholds. *J. Mech. Phys. Solids* 144, 104114 (2020).
35. Denoual, C., Vattre, A., 2016. A phase field approach with a reaction pathways-based potential to model reconstructive martensitic transformations with a large number of variants. *J. Mech. Phys. Solids*, 90, 91-107.
36. K. Bhattacharya, S. Conti, G. Zanzotto, J. Zimmer. Crystal symmetry and the reversibility of martensitic transformations. *Nature*, 428, 55-59, 2004.